Inorganic Chemistry

Effect of the Size and Shape on the Electrocatalytic Activity of Co_3O_4 Nanoparticles in the Oxygen Evolution Reaction

S. Saddeler, U. Hagemann, and S. Schulz*

Read Online

ACCESS | Metrics & More | Article Recommendations | Supporting Information

ABSTRACT: Co_3O_4 nanoparticles were size- and shape-selectively synthesized in a solvothermal approach by the thermal decomposition of either cobalt(II) acetylacetonate $[Co(acac)_2]$ or cobalt(II) nitrate $[Co(NO_3)_2]$ in different solvents followed by calcination under air. Spherical, cubic, octahedral, and platelike nanoparticles with narrow size distributions and sizes ranging from 8 to 90 nm were formed in high yield. The nanoparticles were characterized by X-ray diffraction, scanning and transmission electron microscopy, energy-dispersive X-ray analysis, and X-ray photoelectron spectroscopy. The distinctive influence of the size and shape of the nanoparticles on the electrocatalytic activity in the oxygen evolution reaction is also demonstrated.
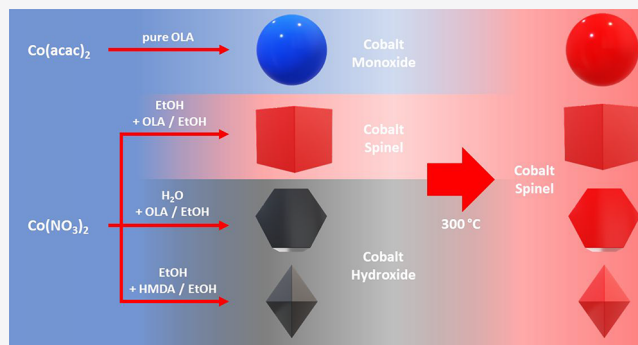
INTRODUCTION

The development of highly efficient electrocatalysts for clean energy production and environmental remediation is crucial in our time. The high energy demand of water electrolyzers due to the sluggish kinetics of both the oxygen evolution reaction (OER) and oxygen reduction reaction (ORR)[1,2] requires catalysts of high efficiency and long-term stability. Unfortunately, standard catalysts including precious-metal electrocatalysts are not only high-cost[3,4] but also monofunctional catalysts; i.e., platinum is highly active in the ORR, but it is only moderately active in the OER, whereas IrO_2 and RuO_2, which are the current benchmarking OER catalysts, are less active in the ORR.[5,6] In this case, a better substitute for noble metals requires the development of highly active and low-cost bifunctional catalysts.

Because of their earth abundance and excellent electrochemical activity, spinel-type mixed-metal oxides are intensively studied for the OER on the anodic side.[7] Because the catalytic activity in the OER generally depends on the number of active sites and the adsorption energies of reactive intermediates, nanoparticles are very attractive candidates. Their catalytic activity often exceeds that of bulk counterparts because of their high surface areas and high number of active sites, as well as their unique electronic and chemical surface properties.[8] These properties can, furthermore, be tuned in various ways, resulting in different electrocatalytic activity and selectivity.[9] For instance, careful adjustment of the nanoparticle size allows one to control the number of low-coordinated sites on the catalyst surface as well as the reactant binding strength, whereas the shape of the nanoparticle may provide certain facets that are favorable for a catalytic reaction.[10] In addition, the stability of the oxide species at the surface, which also affects the activity and selectivity of a reaction, depends on both the shape and size of the nanoparticle, whereas modification of the mixed-metal oxide composition, i.e., variation of the metal-to-metal ratio or the incorporation of additional metals (electronic doping), may provide an optimal ensemble of active sites on the catalyst surface.[11−15]

In order to understand the nano- and microstructural roles of the catalysts on its performance as well as on the reaction mechanisms and kinetics, the synthesis of crystalline (nano)-materials with defined size and morphology, including defined crystallographic surfaces, is mandatory. Size- and shape-selective syntheses of transition-metal spinel-type nanoparticles are typically achieved using a bottom-up approach via the thermal decomposition of molecular precursors such as metal acetylacetonates[16,17] and metal oleate complexes[18] in high-boiling solvents and in the presence of suitable organic surfactants (*capping agents*). We recently reported on the synthesis of spherical $CoFe_2O_4$ spinel-type nanoparticles formed in a solvothermal approach by thermolysis of cobalt(II) acetylacetonate $[Co(acac)_2]$ and iron(III) acetylacetonate $[Fe(acac)_3]$ at different temperatures.[19] With increasing reaction temperature, the size of the nanoparticles increased from 3 nm (200 °C) to 5 nm (250 °C) and finally to 8 nm
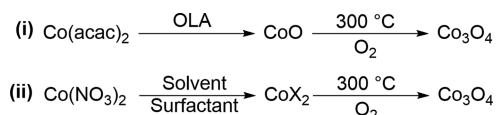
(300 °C), whereas the electrocatalytic activity in the OER was found to steadily decrease with increasing particle size. Coprecipitation of $CoFe_2O_4$ in the presence of different concentrations of sodium dodecyl sulfate yielded particles ranging from 16 to 27 nm in diameter. These nanoparticles showed different electrical properties, with the largest particles showing the largest dielectric constant.[20] Using a coprecipitation method, Pereira et al. reported on the influence of the precipitation agent on the size of the resulting MFe_2O_4 (M = Co, Fe, Mn) nanoparticles.[21] The largest nanoparticles were synthesized using sodium hydroxide, whereas smaller particles were formed upon the addition of organic amines. A seed-mediated growth method was also successfully employed to further increase the size of Fe_3O_4 particles because of the repeated growth processes upon the addition of new precursor material.[22] On the other hand, Hu et al. reported on a solvothermal synthesis of Co_3O_4 nanoparticles with either cubic, hexagonal, or beltlike shapes, which was realized simply by changing the solvent from ethanol (EtOH) to water (H_2O) or glycol.[23] The hexagonal Co_3O_4 plates, for example, were formed in methanol at lower temperatures in comparison to the other morphologies. In addition to a successful synthesis, the authors also proved the promising catalytic properties of the nanoparticles in methane combustion, with the {112}-terminated particles showing the highest catalytic activity. Other morphologies, such as flower-like as well as disc- and cube-shaped Co_3O_4 particles, were synthesized via a poly-(vinylpyrrolidone)-mediated hydrothermal route. The Co_3O_4 nanoflowers showed the best performance in electrochemical lithium storage experiments.[24]

We recently became interested in the size- and shape-selective synthesis of spinel-type nanoparticles after reporting on their use in alcohol oxidation reactions as well as in OERs.[19,25−28] We herein extend our studies on the synthesis of pure Co_3O_4 nanoparticles, while exploring the role of defined sizes and shapes (morphologies) on the electrocatalytic performance of the nanoparticles.

■ RESULTS AND DISCUSSION

Synthesis and Characterization. Co_3O_4 nanoparticles with different sizes and morphologies were synthesized by the thermal decomposition of $Co(acac)_2$ in oleylamine (OLA). Because of the reductive character of OLA,[29] the reaction initially yielded rock-salt-type cobalt(II) oxide (CoO), which was subsequently calcined under air at 300 °C to finally give spinel-type Co_3O_4 (Scheme 1i). The solvothermal approaches using solutions of cobalt(II) nitrate $[Co(NO_3)_2]$ in different solvents (EtOH, H_2O) in the presence of diluted capping agents [OLA in EtOH and hexamethylenediamine (HMDA)

Scheme 1. Synthesis of Co_3O_4 Nanoparticles by Either (i) Thermal Decomposition of $Co(acac)_2$ in OLA Followed by Calcination of the As-Formed CoO at 300 °C under Air or (ii) Solvothermal Synthesis Using Different Combinations of Solvents and Capping Agents of (a) OLA/EtOH in EtOH, (b) OLA/EtOH in H_2O, or (c) HMDA/EtOH in EtOH, Followed by Calcination at 300 °C under Air

(i) $Co(acac)_2 \xrightarrow{\text{OLA}} CoO \xrightarrow[O_2]{300\ °C} Co_3O_4$

(ii) $Co(NO_3)_2 \xrightarrow[\text{Surfactant}]{\text{Solvent}} CoX_2 \xrightarrow[O_2]{300\ °C} Co_3O_4$

in EtOH; Scheme 1ii] either proceeded with the formation of cobalt(II) hydroxide $[Co(OH)_2]$, which was subsequently calcined at 300 °C under air to yield Co_3O_4 nanoparticles, or directly formed the spinel-type cobalt oxide Co_3O_4 (Table 1).

Thermal Decomposition of $Co(acac)_2$ in OLA. The initially formed CoO nanoparticles were characterized by powder X-ray diffraction (PXRD) and transmission electron microscopy (TEM), as shown for sample S1, whereas PXRD and TEM photographs of samples S2−S5 are given in Figures S1 and S2.

Thermal decomposition of $Co(acac)_2$ always yielded spherical rock-salt CoO nanoparticles, as is exemplarily shown for sample S1 (Figure 1a). The size of the nanoparticles increased with increasing amount of precursor [S1, 8 nm (Figure 1b; high-resolution (HR)TEM image displayed in Figure 1c); S2, 9 nm; S3 11 nm; S4 13 nm; S5 15 nm] according to TEM studies (Figure S1). In the preparation of sample S5, we also evaluated the role of the decomposition temperature. According to PXRD (Figure S3), crystalline CoO nanoparticles were formed at 200 °C (S5a), 250 °C (S5), and 300 °C (S5b). The particle size also increased with increasing reaction temperature from 11 nm (S5a) to 15 nm (S5) (Figure S3), whereas sample S5b, formed at 300 °C, showed even larger particles. However, the morphology of the nanoparticles obtained at 300 °C was not as uniform as that of the ones prepared at lower temperatures; aside from spherical nano-particles, cubic and octahedral particles were also observed (Figure S 3d). According to these findings, 250 °C is the upper limit of the optimal reaction temperature.

Calcination of the CoO nanoparticles (samples S1−S5) selectively yielded phase-pure spinel-type Co_3O_4 nanoparticles (samples S1C−S5C; Figure 2a) without any traces of additional crystalline phases, as was proven by Rietvalld refinement (Figure 2b). The lattice parameters of samples S1 (a = 4.267 Å) and S1C (a = 8.078 Å) are in very good agreement with the values reported for CoO (a = 4.263 Å) and Co_3O_4 (a = 8.072 Å), respectively.

On the basis of the particle-size analysis using the Scherrer equation, the size of the nanoparticles was relatively preserved during calcination (Figure S2). For example, a size of 8.8 nm was calculated for the CoO nanoparticles (sample S1), which compares well with the TEM measurements (8 nm; Figure S4, sample S1), while the Co_3O_4 nanoparticles formed by calcination (sample S1C) showed a mean size of 8.1 nm based on the Scherrer equation, which is also in good agreement with the size as-determined by TEM (Figure S4, sample S1C). However, the results from the PXRD experiments should be carefully considered because the increasing particle size with increasing concentration of the $Co(acac)_2$ precursor was clearly identified neither for the CoO nano-particles nor for the Co_3O_4 nanoparticles. As was observed for the CoO nanoparticles (samples S1−S5 in Figure S2), the PXRD patterns of the spinel-type Co_3O_4 nanoparticles (samples S1C−S5C) synthesized with different amounts of precursor (Figure 2a) are almost identical. These findings most likely result from the strong fluorescence effect of cobalt.

Figure 3 shows TEM images of spherical Co_3O_4 nano-particles obtained after calcination (samples S1C−S5C). The particle size was found to increase with increasing precursor concentration from 8 nm (sample S1C in Figure 3a) to 9 nm (sample S2C in Figure 3b) to 11 nm (sample S3C in Figure 3c) to 13 nm (sample S4C in Figure 3d) and finally to 15 nm (sample S5C in Figure 3e), while preserving a spherical shape.

Table 1. Co_3O_4 Samples Synthesized by the Thermal Decomposition of $Co(acac)_2$ or by Solvothermal Approaches Using Solutions of $Co(NO_3)_2$ in Different Solvents

	precursor	mass (g; mmol)	solvent (mL)	surfactant (mL)	temperature (°C)	time (h)	product[a]
S1	$Co(acac)_2$	0.386; 1.5	OLA (7.4)	OLA	250	1	CoO
S2	$Co(acac)_2$	0.771; 3.0	OLA (7.4)	OLA	250	1	CoO
S3	$Co(acac)_2$	1.16; 4.5	OLA (7.4)	OLA	250	1	CoO
S4	$Co(acac)_2$	1.54; 6.0	OLA (7.4)	OLA	250	1	CoO
S5	$Co(acac)_2$	1.93; 7.5	OLA (7.4)	OLA	250	1	CoO
S5a	$Co(acac)_2$	1.93; 7.5	OLA (7.4)	OLA	200	1	CoO
S5b	$Co(acac)_2$	1.93; 7.5	OLA (7.4)	OLA	300	1	CoO
S6	$Co(NO_3)_2$	0.291; 1.0	EtOH (20)	OLA/EtOH (2/10)	180	15	Co_3O_4
S7	$Co(NO_3)_2$	0.291; 1.0	H_2O (20)	OLA/ETOH (2/10)	180	15	$Co(OH)_2$
S8	$Co(NO_3)_2$	0.291; 1.0	EtOH (20)	HMDA/EtOH (708 mg/12)	180	15	$Co(OH)_2$
S9	$Co(NO_3)_2$	0.582; 2.0	EtOH (20)	OLA/EtOH (2/10)	180	15	Co_3O_4

[a]Rock-salt-type CoO as well as $Co(OH)_2$ nanoparticles were subsequently calcined at 300 °C for 1 h, resulting in the formation of phase-pure Co_3O_4 nanoparticles.
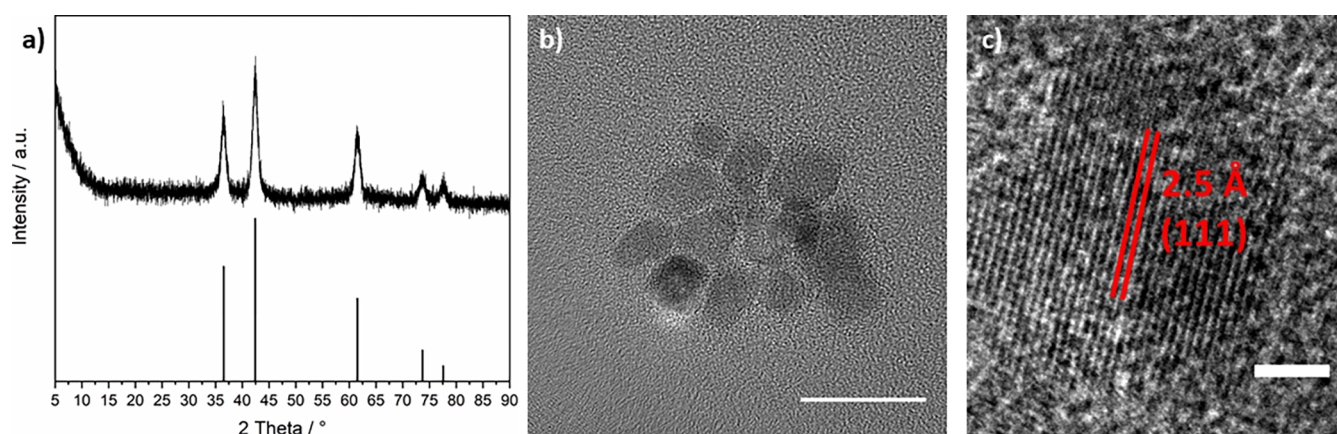

Figure 1. (a) X-ray diffractogram of sample **S1** (CoO; reference PDF 01-071-1178). (b) TEM and (c) HRTEM photographs of sample **S1** (CoO). Scale bars: (b) 20 nm; (c) 2 nm.
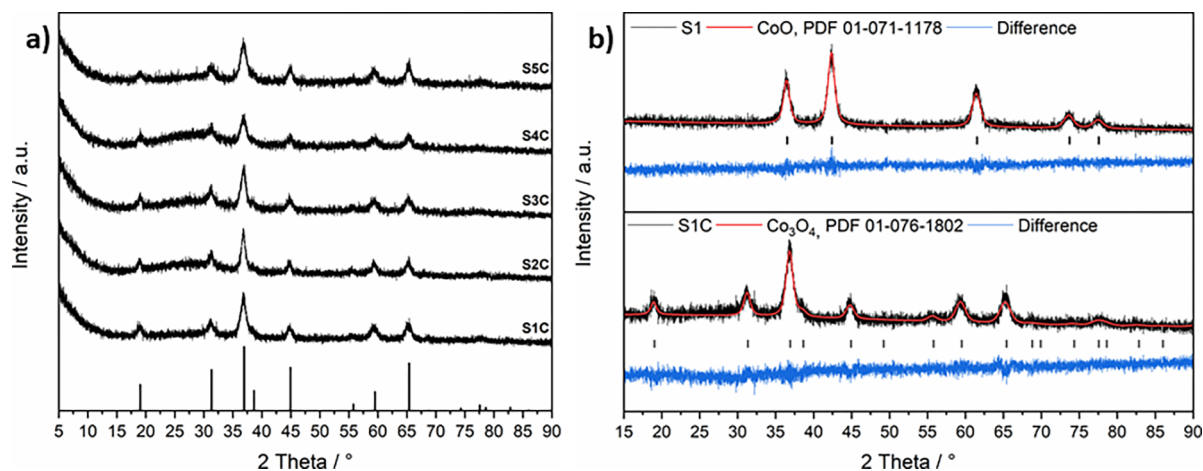

Figure 2. (a) PXRD patterns of Co_3O_4 nanoparticles (samples **S1C–S5C**) formed by the calcination of CoO nanoparticles (samples **S1–S5**; reference for Co_3O_4, PDF 01-076-1802). (b) Rietveld refinement for CoO (**S1**, top) and Co_3O_4 (**S1C**, bottom).

Comparable particle sizes were observed for the original CoO nanoparticles (Figure S4). These results demonstrate that the nanoparticle size is controlled during the precursor decomposition rather than the calcination process and that no significant sintering occurs under such low-temperature calcination conditions (300 °C). Even though a slight broadening of the size distribution was observed for the largest particles, this is most likely due to Ostwald ripening.[30]

The preferred growth of larger nanoparticles with increasing precursor concentration has been previously reported, i.e., for iron oxide nanoparticles.[31,32] Because the nanoparticle growth is diffusion-limited while the diffusion rate itself increases with the precursor concentration, the growth of larger particles with increasing precursor concentration is therefore favored. Sintering of the nanoparticles is typically observed in annealing processes at high temperatures.[33] Figure 3f shows the (311)
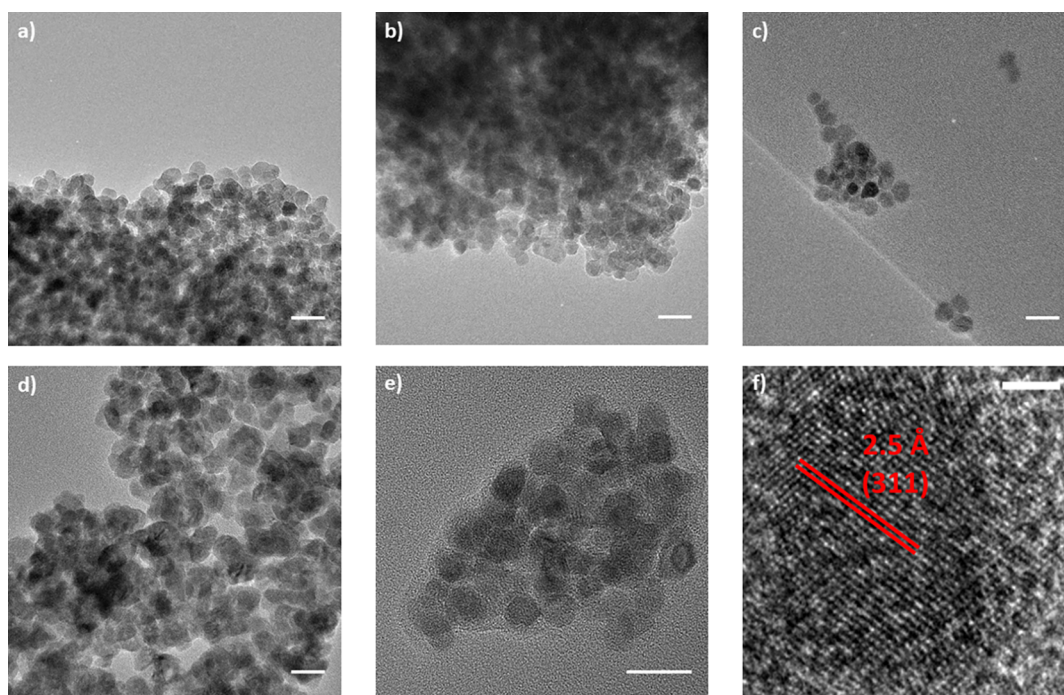
Figure 3. TEM images of (a) 8 nm (**S1C**), (b) 9 nm (**S2C**), (c) 11 nm (**S3C**), (d) 13 nm (**S4C**), and (e) 15 nm (**S5C**) Co_3O_4 nanospheres. (f) HRTEM image of **S5C**. Scale bars: (a−e) 20 nm; (f) 2 nm.
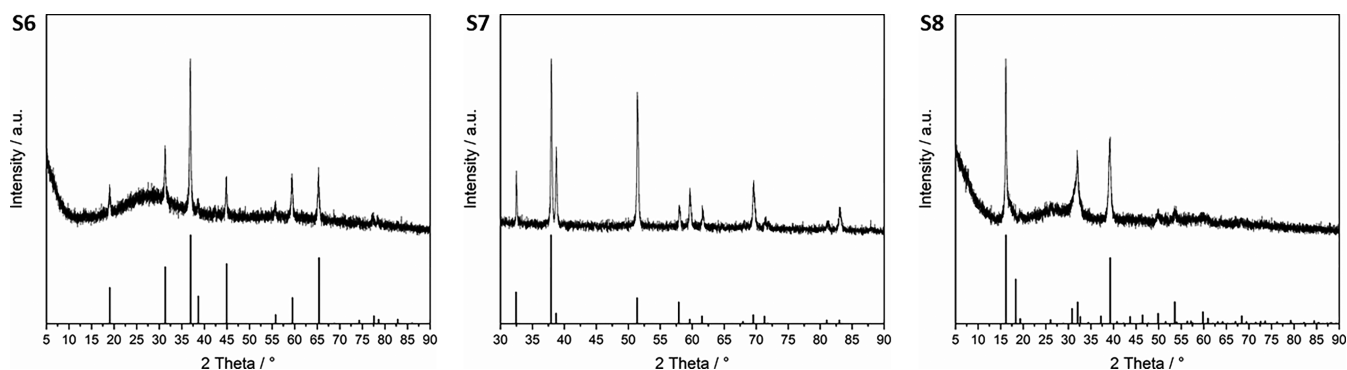

Figure 4. X-ray diffractograms of samples **S6** (cubic Co_3O_4), **S7** (platelike $Co(OH)_2$), and **S8** (octahedral $Co(OH)_2$). References: **S6**, Co_3O_4, PDF 01-076-1802; **S7**, β-$Co(OH)_2$, PDF 01-089-8616; **S8**, $Co_2(OH)_3Cl$, PDF 01-073-2134.

plane with a d spacing of 2.4 Å in sample **S5C**, which is the most exposed crystal plane in the nanospheres, whereas the rock-salt-type CoO nanospheres (sample **S5**) showed the (111) plane. The nonpolar (100) plane of the cubic rock-salt-type structure contains equal numbers of anions (O^{2-}) and cations (Co^{2+}) and therefore represents the ideal termination of the bulk structure. In contrast, the polar (111) plane is hexagonally closest packed and contains only one sort of ions, which renders this termination inherently unstable.[34] However, octahedra and tetrahedra are limited by the (111) plane, and in our case, coordination of the organic capping agents may have a stabilizing effect, resulting in the preferred (111) termination, as observed for the CoO nanoparticles. Thermal treatment of CoO nanoparticles yielded cube-shaped Co_3O_4 nanoparticles with (311) and (220) crystal planes, as was previously reported for Co_3O_4 nanoparticles.[35,36]

Solvothermal Approach. The thermal decomposition of $Co(acac)_2$ at 250 °C only yielded spherical nanoparticles. In order to investigate the effect of the different crystallographic facets of Co_3O_4 on the resulting electrochemical (OER)

activity, we performed shape-selective syntheses of Co_3O_4 nanoparticles using solvothermal reactions of $Co(NO_3)_2$ in different solvents (EtOH and H_2O) and with different (diluted) capping agents (OLA in EtOH and HMDA in EtOH).

All solvothermal reactions using solutions of $Co(NO_3)_2$ in EtOH and H_2O with diluted capping agents (OLA or HMDA in EtOH) initially yielded green precipitates upon the addition of the surfactant/solvent mixture. Instead of formation of a rock-salt cobalt(II) oxide phase as was observed upon thermal decomposition of $Co(acac)_2$ in pure OLA, the resulting precipitates from reactions in H_2O/OLA (sample **S7** in Figure 4) and EtOH/HMDA (sample **S8** in Figure 4) were transformed into a cobalt hydroxide phase upon thermal treatment to 180 °C, as shown by PXRD (Figure 4). In remarkable contrast, the reaction in EtOH/OLA directly yielded Co_3O_4 nanoparticles (sample **S6** in Figure 4).

Although thermal decomposition methods of metal acetylacetonates are commonly reported in the literature, no general decomposition pathway can be derived from these

studies. For instance, $Zn(acac)_2$ and $Fe(acac)_3$ decompose in the solid state under an inert gas atmosphere via a carbonate intermediate, yielding the corresponding metal oxides ZnO and Fe_2O_3, respectively.[37,38] In contrast, the thermal decomposition of $Co(acac)_2$ under vacuum releases acetone and carbon dioxide, while yielding a solid product described as "amber" and "some green material" depending on the decomposition temperature; this description coincides with the color of CoO.[39] In contrast, $Co(acac)_3$ was found to decompose upon thermal treatment with intermediate formation of $Co(acac)_2$, which consequently reacts with oxygen, with the formation of cobalt acetate $[Co(OAc)_2]$.[40] The formation of acac radicals might also play an important role in the thermolysis of transition-metal tris-(acetylacetonates),[41] Finally, thermolysis of $Co(OAc)_2$ at 280 °C yielded rock-salt-type CoO, as proven by PXRD,[42] which corresponds to our findings observed for the thermolysis of $Co(acac)_2$ in OLA at a comparable reaction temperature (samples **S1−S5**).

In remarkable contrast to the findings observed with $Co(acac)_2$, the treatment of $Co(NO_3)_2$ in an alkaline solution at much lower temperatures (45 °C) proceeded via the formation of $Co(OH)_2$, which is then transformed into either CoO(OH) or Co_3O_4 depending on the oxidation source [30% H_2O_2 for oxidation of CoO(OH) or air at 400 °C for oxidation of Co_3O_4].[43] Markov et al. reported on the thermolysis of $Co(OH)_2$ under an air atmosphere, which initially gave CoO(OH) as a reaction intermediate, which was subsequently transformed into Co_3O_4 upon thermal treatment at 280 °C (Scheme 2).[44] The formation of CoO was not observed during

Scheme 2. Thermolysis of $Co(OH)_2$ in Air

$$Co(OH)_2 \xrightarrow[O_2]{\Delta} CoO(OH) \xrightarrow[O_2]{\Delta} Co_3O_4$$
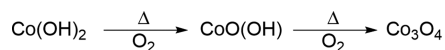
this process; this agrees with our observations for the solvothermal approach. We therefore conclude that the formation of Co_3O_4 nanocubes (sample **S6**) results from the decomposition of $Co(OH)_2$ as the reaction intermediate formed during this synthesis.

Figure 5 shows TEM photographs of the resulting nanoparticles (samples **S6−S8**) directly after solvothermal synthesis, which demonstrate the influential role of the solvent and surfactant on the morphology of the nanoparticles. While cubic Co_3O_4 nanoparticles (sample **S6** in Figure 5) were directly formed by reaction in EtOH/OLA, platelike and

octahedral $Co(OH)_2$ nanoparticles were formed in H_2O/OLA (sample **S7** in Figure 5) and EtOH/HMDA (sample **S8** in Figure 5), respectively. The octahedral $Co(OH)_2$ particles (sample **S8**) most likely contain organic surfactants that could not be removed in the washing steps. Obviously, the solvent and surfactant used in the solvothermal process have a large influence not only on the resulting crystallographic phase of the nanoparticles $[Co(OH)_2$ vs $Co_3O_4]$ but also on the nanoparticle morphology. The formation of very large hexagonal platelike particles likely results from the poor solubility of OLA in the EtOH/H_2O mixture. As was previously reported for metal nanoparticles,[45,46] such conditions ultimately lead to a growth mechanism at the interface of the two-phase mixture of OLA and EtOH/H_2O.

The mean size of the cubic Co_3O_4 nanoparticles (sample **S6**, 17 nm) increased with the use of larger amounts of the precursor (sample **S9**, 30 nm); however, the morphology became less defined (Figure S5). The size of the octahedral $Co(OH)_2$ nanoparticles (sample **S8**, 35 nm) was much smaller than that of the hexagonal plates (sample **S7**), whose size ranged from nanometers to several micrometers. Smaller hexagonal plates were also observed, which typically stick on the surface of the larger plates (sample **S7** in Figure 5).

The cobalt(II) hydroxides (samples **S7** and **S8**) were then calcined under air at 300 °C for 1 h, yielding the expected spinel-type Co_3O_4 phases, as proven by PXRD (Figure 6). The cubic Co_3O_4 nanoparticles (sample **S6**) were also calcined to prove whether this process has any influence on the crystallography and morphology of the Co_3O_4 nanoparticles.

The sizes of the Co_3O_4 nanocubes before annealing (sample **S6**, 17 nm) and after annealing at 300 °C in air (**S6C**, 16 nm; Figure 7a) are almost identical. The nanocubes are terminated by the (220) plane (Figure 7b), whereas the edges represent the cubic planes {100}, {010}, and {001}, as previously reported.[23] The original morphology and mean size of the octahedral $Co(OH)_2$ nanoparticles (sample **S8**, 35 nm) were both preserved upon calcination only to give octahedral Co_3O_4 nanoparticles (sample **S8C**, 36 nm; Figure 7c). These octahedral Co_3O_4 nanoparticles are terminated by the (111) plane with a *d* spacing of 4.7 Å (Figure 7d), which agrees with previous reports on spinel-type mixed-metal octahedral nanoparticles.[47] Because octahedra naturally grow from cubes via the overgrowth of cubic planes that result in (111) facets,[48] the use of HMDA instead of OLA for the nanocubes should favor the growth rate.
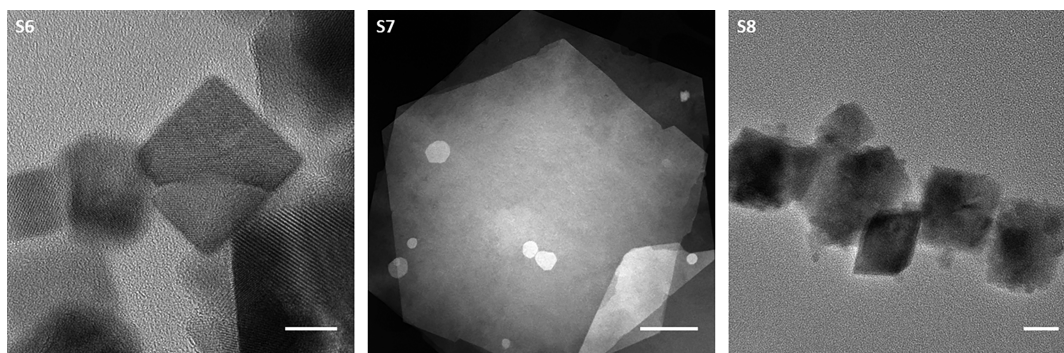

Figure 5. TEM photographs of samples **S6** (cubic Co_3O_4), **S7** [platelike $Co(OH)_2$], and **S8** [octahedral $Co(OH)_2$]. Scale bars: **S6**, 10 nm; **S7**, 1 μm; **S8**, 20 nm.
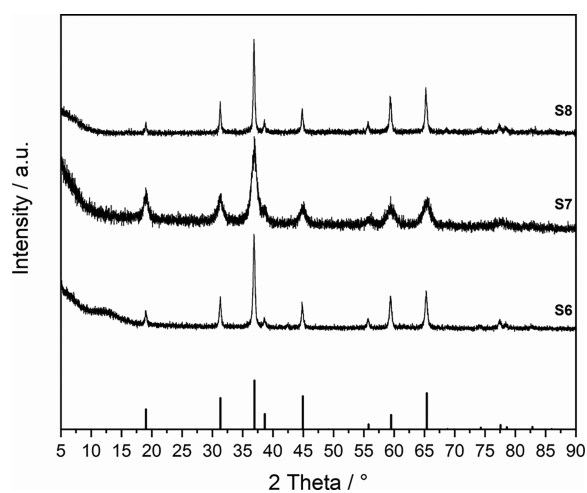
Figure 6. PXRD patterns of samples **S6** (cubic Co_3O_4), **S7** (platelike Co_3O_4), and **S8** (octahedral Co_3O_4). Reference for Co_3O_4: PDF 01-076-1802.

Calcination of platelike $Co(OH)_2$ nanoparticles (sample **S7**) also occurred with preservation of the morphology, yielding hexagonal platelike Co_3O_4 nanoparticles (sample **S7C**), as proven by selected-area X-ray diffraction (SAED). As was also observed for the calcined Co_3O_4 sample (Figure S7), the $Co(OH)_2$ particles show the same hexagonal shape with a diffraction pattern fitting to cobalt hydroxide (PDF 01-089-8616). The SEM image shows the hexagonal morphology of these large particles, which have diameters of several micrometers (Figure 8a). Some of the smaller particles sitting on top of the larger ones are also visible in the SEM and TEM

photographs (Figure 8b). The thicknesses of the Co_3O_4 hexagons range from 60 to 90 nm irrespective of the plate diameter. Depending on the direction on the surface, two dominant facets are visible: the (222) and (220) planes with lattice spacings of 2.3 and 2.9 Å, respectively (Figure 8c).

X-ray Photoelectron Spectroscopy (XPS) Characterization. A XPS survey scan of sample **S1C** exclusively shows the existence of cobalt, oxygen, and carbon on the sample surface (Figure 9a). The amount of carbon was found to vary in different samples, but no correlation between the carbon intensity and the catalytic activity of the samples was observed. XPS spectra of different Co_3O_4 nanoparticles with different morphologies show the typical pattern for the cobalt spinel in the Co 2p spectra (Figure 9b).[49]

In the Co $2p_{3/2}$ region (around 780 eV), an asymmetric peak is visible because of the presence of Co^{3+} ions. The satellite peak at 788 eV is less defined compared to CoO, which only contains Co^{2+} ions[50,51] and is shifted to higher binding energies. The shape of the Co 2p signal is similar for all four samples, and no increase of the Co^{2+} intensity is found (Figure S10). Therefore, the total change of the Co^{2+} content on the surface of the samples is less than about 10% of the total cobalt amount. Any larger variation would result in a different Co 2p peak shape, which should be visible considering the signal-to-noise ratio. The O 1s spectra of all samples (Figure 9c) show an intense peak of the lattice oxygen at 530 eV, whereas the peak at 532 eV indicates the presence of hydroxide or oxyhydroxide groups on the surface.[52] The octahedral nanoparticles (sample **S8C**) and, to a lesser extent, the spherical (sample **S1C**, 8 nm) and hexagonal nanoparticles (sample **S7C**) each show a distinct additional peak with low intensity at a binding energy of 534 eV, indicated by the two
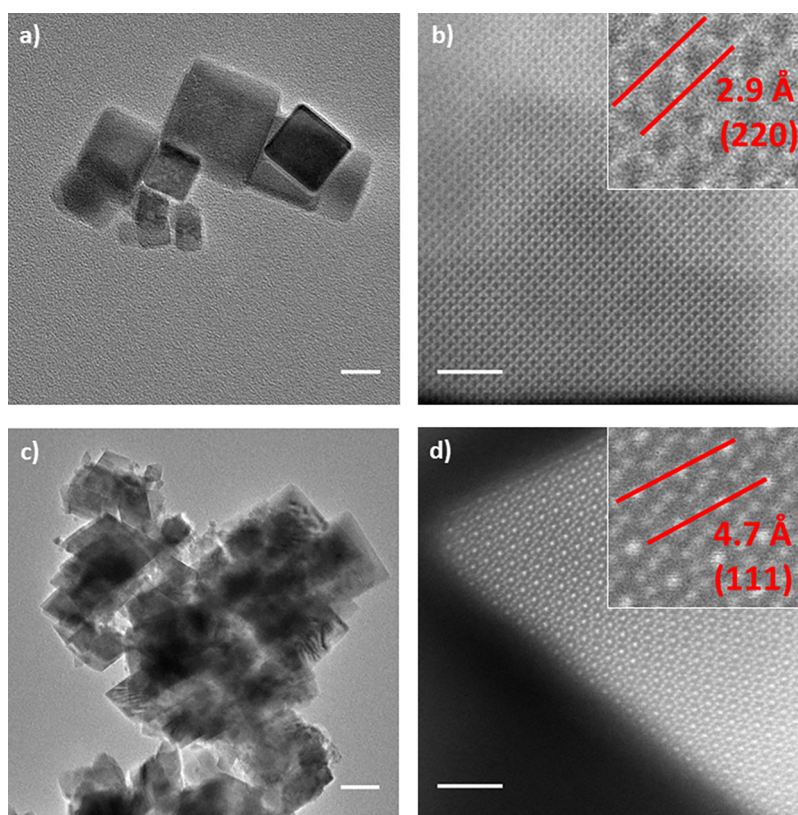

Figure 7. TEM images of annealed samples **S6C** (a and b) and **S8C** (c and d). Scale bars: (a) 20 nm; (b) 2 nm; (c) 50 nm; (d) 2 nm.
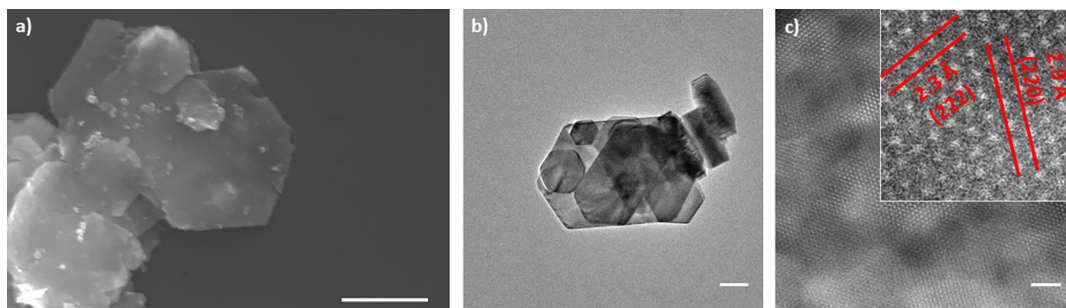
Figure 8. SEM (a) and TEM images (b and c) of sample **S7C** (Co_3O_4, hexagonal plates). Scale bars: (a) 5 μm; (b) 100 nm; (c) 2 nm.
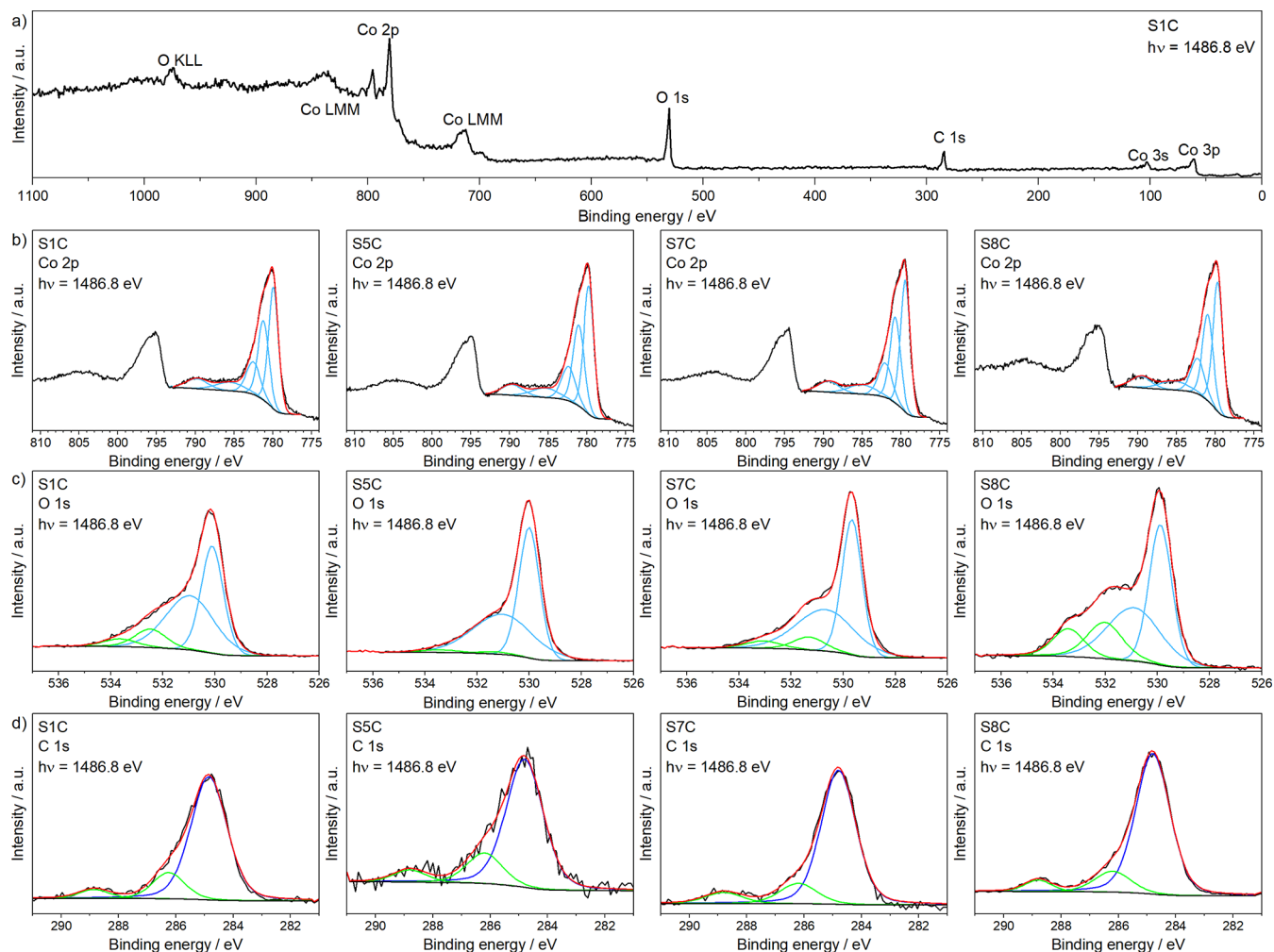

Figure 9. (a) XPS survey scan of sample **S1C**. High-resolution XPS spectra of samples **S1C**, **S5C**, **S7C**, and **S8C**: (b) Co 2p; (c) O 1s; (d) C 1s.

green Gaussian−Lorentzian lines. This peak is only barely visible for the larger spherical particles (sample **S5C**, 15 nm). These signals correlate to the larger amount of carbon and, hence, indicate the presence of different carbon−oxygen bonds (green lines) visible in the C 1s spectra of these samples (Figure 9d).

OER Characterization. OER analyses show no impact of the particle size on the overpotential measured for the rock-salt-type CoO nanoparticles (samples **S1**−**S5** in Figure 10a), whereas a size effect is observed for the annealed spinel-type Co_3O_4 nanoparticles (samples **S1C**−**S5C** in Figure 10b). The current densities were calculated using the geometrical surface (0.196 cm^2). In the Nyquist plots, a minimum charge-transfer

resistance of 335 Ω was found for the 11-nm-sized particles (**S3C**), which correlates with the lowest overpotential measured for sample **S3C**. For slightly higher overpotentials (samples **S4C** and **S5C**), the charge-transfer resistance increases (Figure 10c). Interestingly, the overpotential decreased from 494 to 448 mV with increasing particle size from 8 to 11 nm but then stayed almost constant with further size increase (13 and 15 nm; Figure 10d). Comparable values were previously reported for cobalt spinels.[53] An increase in the catalytic activity is generally expected with decreasing particle size because of the increase of the surface-to-volume ratio. Because we observed an opposite trend in our studies, we conclude that the catalytic activity is largely influenced by
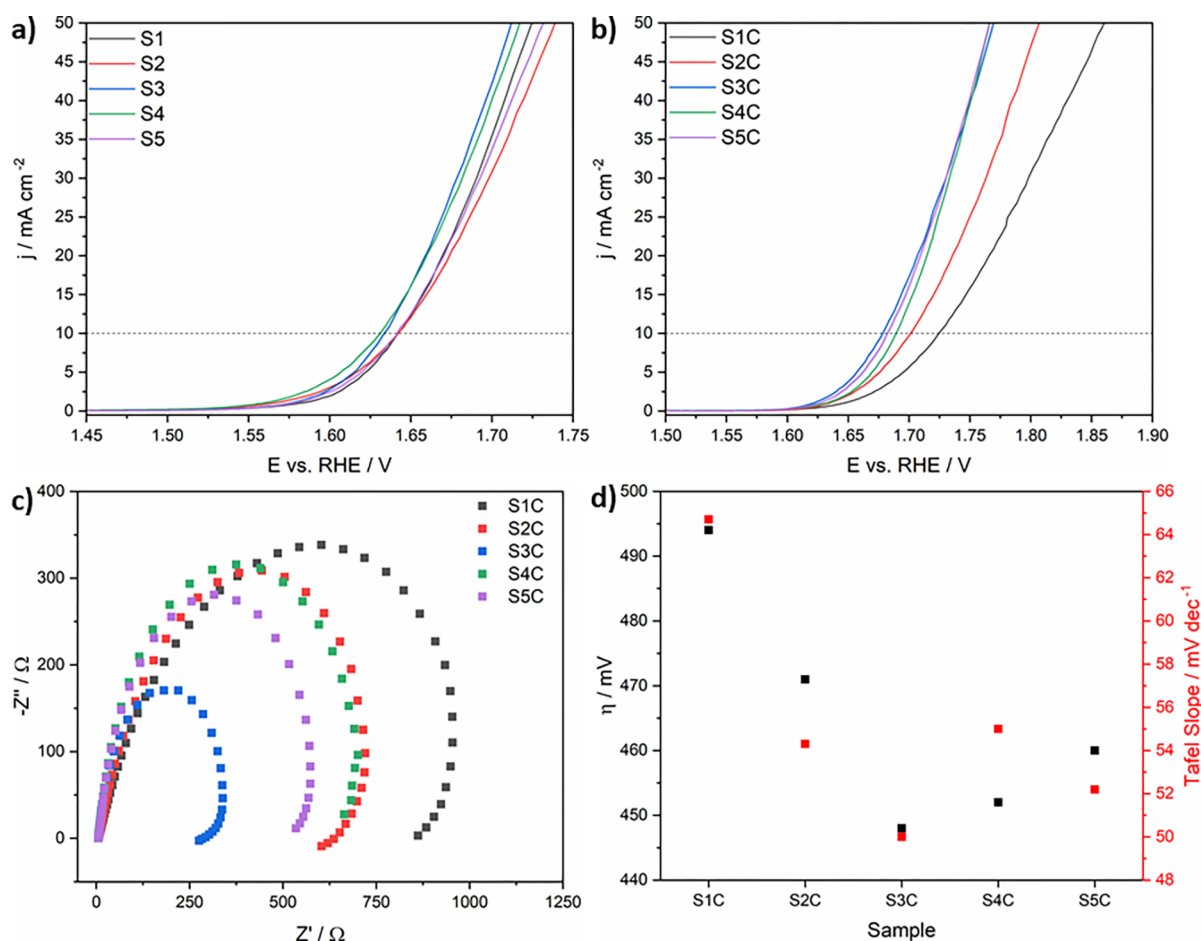
Figure 10. LSV curves for different sizes of spherical (a) CoO (samples **S1−S5**) and (b) Co_3O_4 (samples **S1C−S5C**) formed by the thermal decomposition of $Co(acac)_2$ in OLA (samples **S1−S5**), followed by calcination of the as-formed CoO at 300 °C under air (samples **S1C−S5C**). Nyquist plot (c) and overview (d) for Co_3O_4 nanospheres (samples **S1C−S5C**).

other effects, i.e., the surface modification such as the presence of surfactants/capping agents or oxygen defects, which will be further investigated in the future. Another possible explanation for this phenomenon is that the annealing step is a diffusion-controlled process in which the oxidation of Co^{2+} to Co^{3+} takes place. The larger the particle size, the less Co^{3+} ions can be generated due to slower diffusion rates, which finally leads to substoichiometric Co^{2+}-rich cobalt spinels of the type $Co^{2+}_xCo^{3+}_yO_4$ ($x > 2$ and $y < 1$). Because the presence of Co^{2+} in cobaltite materials positively effects the OER activity,[54] the larger particles show lower overpotentials. Furthermore, the substochiometric Co^{2+} in the cobalt spinel can affect the number of oxygen atoms in the spinel lattice because of incomplete oxidation of Co^{2+} to Co^{3+}, which then leads to oxygen defects in the spinel ($Co_3O_{4−x}$). The presence of oxygen defects would enhance the activity in the OER by lowering the reaction barrier (overpotential).[55]

The same trend observed for the overpotential of samples **S1C−S5C** is true for the Tafel slopes (*iR*-corrected), which decrease from 65 to 50 mV dec$^{−1}$ with increasing particle size, indicating a slight change of the reaction mechanism. Suen et al.[56] investigated the correlation between the Tafel slope and the mechanism for the OER. According to their reports, a slope of 60 mV dec$^{−1}$ is commonly found for mechanisms in which the reaction following the first electron transfer is rate-determining. For lower slopes (30 mV dec$^{−1}$), the third electron transfer becomes the rate-determining step. On the

basis of these findings, the mechanism of our reactions changes only slightly in the direction of the third transfer as the rate-limiting step for particles with sizes of ≥11 nm. Nevertheless, the first electron transfer is still rate-determining for all Co_3O_4 nanospheres.

The linear-sweep voltammetry (LSV) curves for the OER of differently shaped Co_3O_4 nanoparticles (Figure 11a) show that the lowest overpotential belongs to the hexagonal plates (sample **S7C**, 430 mV). A slightly weaker activity was observed for the 16 nm cubes (sample **S6C**) and the 15 nm spherical particles (sample **S5C**), which are in the same range with overpotentials of 450 and 460 mV, respectively. The larger nanocubes (sample **S9C**) are less active in OER catalysis in comparison to the smaller ones (sample **S6C**), which fits with the characteristic of a lower surface-to-volume ratio. The higher activity of the hexagonal Co_3O_4 plates (sample **S7C**) compared to the Co_3O_4 nanocubes (sample **S6C**) is in good agreement with the results reported by Sidhureddy et al.[36] The highest overpotential was found for the Co_3O_4 octahedra (sample **S8C**, 529 mV). This trend leads to the conclusion that the {222} termination, which is predominantly observed in the Co_3O_4 hexagonal plates (sample **S7C**), brings the highest activity for the OER, whereas the (220) plane-terminated Co_3O_4 nanocubes (sample **S6C**) are less active. A comparable (low) activity was observed for the spherical particles (samples **S1C−S5C**), which are predominantly (311)-terminated. In
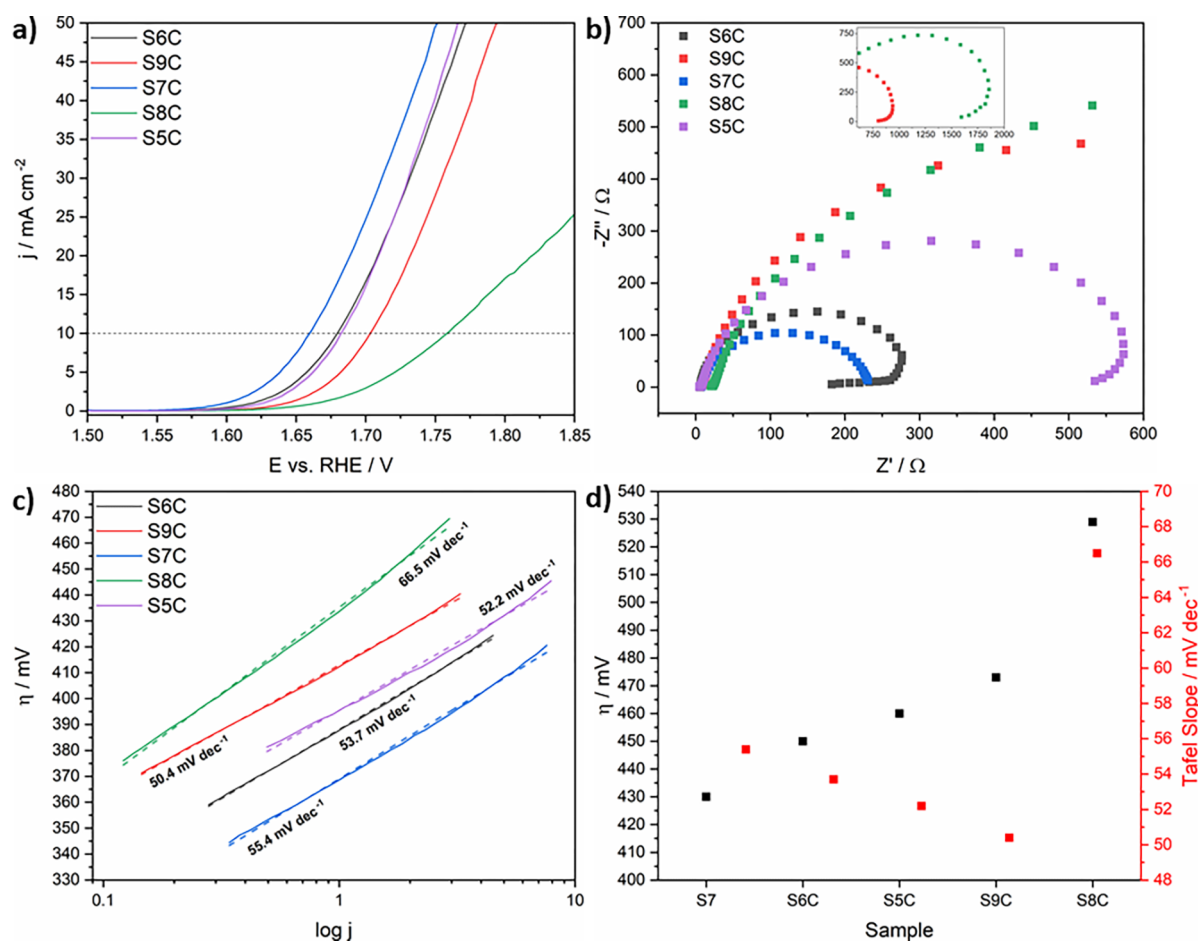
Figure 11. LSV curves for different Co_3O_4 morphologies (a) with a Nyquist plot (b), a Tafel plot (c), and an overview (d).
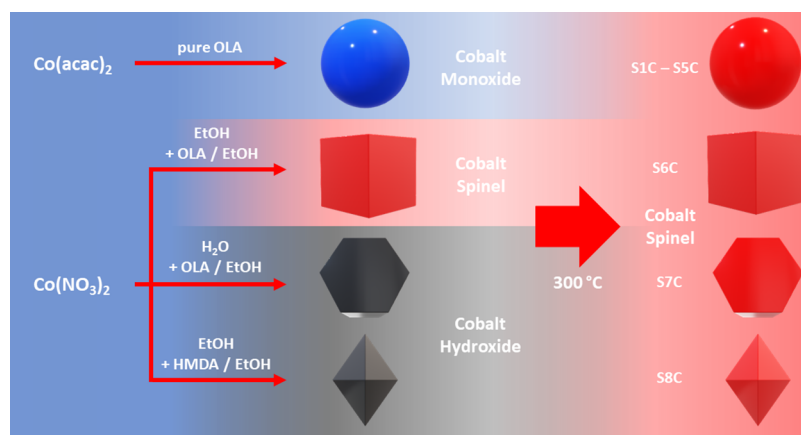

Figure 12. Shape-selective synthesis of Co_3O_4 nanoparticles.

contrast, the (111) plane is the less active facet in Co_3O_4 spinels.

The Nyquist plots (Figure 11b) show the lowest charge-transfer resistance for the most active OER catalyst (hexagonal plates, sample **S7C**) with 225 Ω at 550 mV overpotential. In general, the trend in resistance is comparable to the trend observed for the OER activity, with resistances of 283 Ω for 16 nm cubes (sample **S6C**), 576 Ω for 15 nm spheres (sample **S5C**), 938 Ω for 30 nm cubes (sample **S9C**), and the highest resistance of 1857 Ω for the octahedra (sample **S8C**). The Tafel slopes for samples **S1C−S5C** are almost identical and

only change from 50 to 55 mV dec^{-1} except for the octahedra (sample **S8C**), which show a Tafel slope of 65 mV dec^{-1} (Figure 11c). However, even this change is not significant, and these findings therefore indicate only a slightly different mechanism for the octahedral particles compared to the other shapes (Figure 11d).

■ CONCLUSION

In summary, Co_3O_4 nanoparticles with different morphologies, ranging from spherical (samples **S1C−S5C**) to cubic (sample **S6C**) to octahedral (sample **S8C**) to platelets (sample **S7C**),

as well as different sizes were formed in two different synthetic approaches using different precursors, precursor concentrations, solvents, and surfactants. CoO nanoparticles (samples **S1−S5**), which were initially formed in the thermal decomposition of $Co(acac)_2$ in pure OLA, as well as cobalt hydroxide particles (samples **S7** and **S8**), formed in solvothermal approaches in different solvents and different surfactants, were transformed into the corresponding Co_3O_4 nanoparticles with preservation of their size and morphology (Figure 12). The most dominant facet observed for the Co_3O_4 nanocubes (sample **S6C**) is the (220) facet, whereas the octahedra (sample **S8C**) are terminated by the (111) facet and the hexagonal plates (sample **S7C**) by the (222) and (220) planes.

Spherical CoO nanoparticles (samples **S1−S5**) showed no impact of the particle size on the overpotential, whereas a size effect was observed for spherical Co_3O_4 nanoparticles (samples **S1C−S5C**) and the 11-nm-sized nanoparticles (sample **S1C**) turned out to be the most active catalyst. Surprisingly, the OER analyses did not show a linear relationship between the size of the spherical nanoparticle and its overpotential because the catalytic activity was found to increase from 8- to 11-nm-sized nanoparticles and then stayed almost constant. In contrast, the OER activity was influenced to a larger extent by the morphology of the nanoparticles by increasing in the following trend: hexagons (sample **S7C**) > cubes/spheres (sample **S6C**/ **S5C**) > octahedra (sample **S8C**). From these findings, we conclude that the OER activity is largely influenced by the surface termination, (222) > (220) ≥ (311) > (111), even though other effects such as oxygen defects on the surface may also play an important role in the catalytic OER. Further investigations are currently being performed to address this specific topic.

■ EXPERIMENTAL SECTION

Materials. Cobalt(II) acetylacetonate $[Co(acac)_2$; 99%], hexamethylendiamine (HMDA; 98%), and oleylamine (OLA; ≥98%) were purchased from Sigma-Aldrich. Cobalt(II) nitrate hexahydrate (99%) was purchased from abcr GmbH. All materials were used as received, without further purification.

General Synthesis of Co_3O_4 Nanospheres. A defined mass of $Co(acac)_2$ (Table S1) was suspended in 6 g of OLA and degassed at 120 °C for 1 h. The mixture was stirred at 250 °C for 1 h and then cooled to ambient temperature, yielding CoO nanoparticles, which precipitate upon the addition of ethanol (EtOH; 14 mL). As-formed CoO nanoparticles were isolated by centrifugation (3000 rpm, 10 min) and purified by repeated (two times) redispersion in DCM, followed by precipitation with EtOH and drying in a vacuum. The CoO particles were then converted into Co_3O_4 by calcination at 300 °C in air for 1 h.

Synthesis of Co_3O_4 Nanocubes. A solution of 2 mL of OLA and 10 mL of EtOH was added dropwise to a stirred solution of 291 mg (1.00 mmol) of $Co(NO_3)_2 \cdot 6H_2O$ in 20 mL of EtOH. The resulting mixture was then transferred into a 50 mL stainless-steel autoclave with a Teflon inset and heated in an electrical furnace to 180 °C for 15 h. The resulting precipitate was isolated via centrifugation (3000 rpm, 10 min), washed two times with EtOH, and dried at ambient temperature. The resulting powder was calcined at 300 °C in air for 1 h.

Synthesis of Co_3O_4 Octahedra. Co_3O_4 octahedra were synthesized in a procedure similar to that applied for the nanocube synthesis by the addition of 708 mg (6.09 mmol) of HMDA in 12 mL of EtOH to a solution of $Co(NO_3)_2 \cdot 6H_2O$ in EtOH. The resulting particles were then calcined at 300 °C in air for 1 h.

Synthesis of Co_3O_4 Hexagonal Plates. Co_3O_4 hexagons were synthesized in a procedure similar to that applied for the nanocube

synthesis by dissolving $Co(NO_3)_2 \cdot 6H_2O$ in H_2O instead of EtOH. The resulting particles were then calcined at 300 °C in air for 1 h.

Structural Characterization. Powder X-ray diffraction (PXRD) patterns were measured at ambient temperature with a Bruker D8 Advance powder diffractometer in Bragg−Brentano geometry with Cu Kα radiation (λ = 1.5418 Å, 40 kV, and 40 mA). The powder samples were investigated in the range 5−90°. The size and morphology of the nanoparticles were characterized by using a JEOL 2200FS transmission electron microscope. Energy-dispersive X-ray spectroscopy (EDX) studies were performed using a JEOL JSM6510 scanning electron microscope equipped with an energy-dispersive X-ray detector (Bruker Quantax 400). The obtained spectra were quantified by using the software *Esprit 1.9* (Bruker). X-ray photoelectron spectroscopy (XPS) was recorded by using a ULVAC-Phi Versaprobe II TM spectrometer with a small minimal beam size of 100 μm and a spectral resolution of 0.5 eV.

Electrochemical Characterization. The electrochemical measurements were performed in a three-electrode system consisting of a glassy carbon electrode with a surface area of 0.196 cm^2 as the working electrode, Ag/AgCl (3 M KCl) as the reference electrode, and a platinum sheet as the counter electrode using an Autolab PGSTAT204 potentiostat/galvanostat coupled to a Metrohm rotating-disk-electrode (RDE) rotator. All OER measurements were performed in 1 M KOH. The measured potential was converted to a reversible hydrogen electrode (RHE) by the equation $E_{RHE} = E_{Ag/AgCl}$ + 0.207 V + 0.826 V for pH = 14 at 25 °C.

A total of 5.00 mg of the catalyst was dispersed in 10 μL of Nafion (5 wt %) and a 1:1 mixture of 990 μL of H_2O and EtOH by ultrasonification for 30 min. The as-prepared catalyst ink was drop-coated onto a polished RDE with a mass loading of 100 μg cm^{-2} by using the geometrical surface area and dried at ambient temperature. Prior to the OER measurement, the electrode was cycled at 50 mV s^{-1} in a potential window from 0 to 0.8 V versus Ag/AgCl until constant voltammograms were obtained. OER measurements were performed at 5 mV s^{-1} in a potential window from 0 to 0.8 V versus Ag/AgCl. Electrochemical impedance spectroscopy was performed at frequencies between 100 kHz and 0.1 Hz with an overpotential of 550 mV. The resistance of the electrolyte was determined from the Nyquist plot by using the equation $E_{iR} = E_m − iR$, where E_{iR} is the iR-corrected potential and E_m is the measured potential.

■ ASSOCIATED CONTENT

ⓢ Supporting Information

The Supporting Information is available free of charge at https://pubs.acs.org/doi/10.1021/acs.inorgchem.0c01180.

> Experimental and analytical details (TEM, PXRD, XPS, and SAED images) as well as size distributions of the different nanoparticles (PDF)

■ AUTHOR INFORMATION

Corresponding Author

S. Schulz − *Faculty of Chemistry, University of Duisburg-Essen and Center for Nanointegration Duisburg-Essen, D-45117 Essen, Germany;* ⓞ orcid.org/0000-0003-2896-4488; Email: stephan.schulz@uni-due.de

Authors

S. Saddeler − *Faculty of Chemistry, University of Duisburg-Essen and Center for Nanointegration Duisburg-Essen, D-45117 Essen, Germany*

U. Hagemann − *Interdisciplinary Center for Analytics on the Nanoscale (ICAN), NanoEnergieTechnikZentrum, D-47057 Duisburg, Germany;* ⓞ orcid.org/0000-0002-1880-6550

Complete contact information is available at:
https://pubs.acs.org/10.1021/acs.inorgchem.0c01180

■ REFERENCES

(1) Hou, J.; Wu, Y.; Zhang, B.; Cao, S.; Li, Z.; Sun, L. Rational Design of Nanoarray Architectures for Electrocatalytic Water Splitting. *Adv. Funct. Mater.* **2019**, *29*, 1808367.

(2) Dou, S.; Tao, L.; Huo, J.; Wang, S.; Dai, L. Etched and doped Co_9S_8/graphene hybrid for oxygen electrocatalysis. *Energy Environ. Sci.* **2016**, *9*, 1320−1326.

(3) Walter, M. G.; Warren, E. L.; McKone, J. R.; Boettcher, S. W.; Mi, Q.; Santori, E. A.; Lewis, N. S. Solar Water Splitting Cells. *Chem. Rev.* **2010**, *110*, 6446−6473.

(4) Zou, X.; Zhang, Y. Noble metal-free hydrogen evolution catalysts for water splitting. *Chem. Soc. Rev.* **2015**, *44*, 5148−5180.

(5) Liu, Q.; Wang, Y.; Dai, L.; Yao, J. Scalable Fabrication of Nanoporous Carbon Fiber Films as Bifunctional Catalytic Electrodes for Flexible Zn-Air Batteries. *Adv. Mater.* **2016**, *28*, 3000−3006.

(6) McCrory, C. C. L.; Jung, S.; Peters, J. C.; Jaramillo, T. F. Benchmarking Heterogeneous Electrocatalysts for the Oxygen Evolution Reaction. *J. Am. Chem. Soc.* **2013**, *135*, 16977−16987.

(7) Gu, X. K.; Samira, S.; Nikolla, E. Oxygen Sponges for Electrocatalysis: Oxygen Reduction/Evolution on Nonstoichiometric Mixed Metal Oxides. *Chem. Mater.* **2018**, *30*, 2860−2872.

(8) Gonçalves, J. M.; Matias, T. A.; Toledo, K. C. F.; Araki, K. Electrocatalytic materials design for oxygen evolution reaction. *Adv. Inorg. Chem.* **2019**, *74*, 241−303.

(9) Mistry, H.; Varela, A. S.; Kühl, S.; Strasser, P.; Cuenya, B. R. Nanostructured electrocatalysts with tunable activity and selectivity. *Nat. Rev. Mater.* **2016**, *1*, 1−14.

(10) Wei, C.; Sun, S.; Mandler, D.; Wang, X.; Qiao, S. Z.; Xu, Z. J. Approaches for measuring the surface areas of metal oxide electrocatalysts for determining their intrinsic electrocatalytic activity. *Chem. Soc. Rev.* **2019**, *48*, 2518−2534.

(11) Smith, R. D. L.; Prévot, M. S.; Fagan, R. D.; Zhang, Z.; Sedach, P. A.; Siu, M. K. J.; Trudel, S.; Berlinguette, C. P. Photochemical Route for Accessing Amorphous Metal Oxide Materials for Water Oxidation Catalysis. *Science* **2013**, *340*, 60−63.

(12) Landon, J.; Demeter, E.; İnoğlu, N.; Keturakis, C.; Wachs, I. E.; Vasić, R.; Frenkel, A. I.; Kitchin, J. R. Spectroscopic Characterization of Mixed Fe−Ni Oxide Electrocatalysts for the Oxygen Evolution Reaction in Alkaline Electrolytes. *ACS Catal.* **2012**, *2*, 1793−1801.

(13) Fominykh, K.; Chernev, P.; Zaharieva, I.; Sicklinger, J.; Stefanic, G.; Döblinger, M.; Müller, A.; Pokharel, A.; Böcklein, S.; Scheu, C.; Bein, T.; Fattakhova-Rohlfing, D. Iron-doped nickel oxide nanocrystals as highly efficient electrocatalysts for alkaline water splitting. *ACS Nano* **2015**, *9*, 5180−5188.

(14) Zou, S.; Burke, M. S.; Kast, M. G.; Fan, J.; Danilovic, N.; Boettcher, S. W. Fe (Oxy)hydroxide Oxygen Evolution Reaction Electrocatalysis: Intrinsic Activity and the Roles of Electrical Conductivity, Substrate, and Dissolution. *Chem. Mater.* **2015**, *27*, 8011−8020.

(15) Calle-Vallejo, F.; Díaz-Morales, O. A.; Kolb, M. J.; Koper, M. T. M. Why Is Bulk Thermochemistry a Good Descriptor for the Electrocatalytic Activity of Transition Metal Oxides? *ACS Catal.* **2015**, *5*, 869−873.

(16) Sathya, A.; Guardia, P.; Brescia, R.; Silvestri, N.; Pugliese, G.; Nitti, S.; Manna, L.; Pellegrino, T. $Co_xFe_{3−x}O_4$ Nanocubes for Theranostic Applications: Effect of Cobalt Content and Particle Size. *Chem. Mater.* **2016**, *28*, 1769−1780.

(17) Zhang, K.; Zuo, W.; Wang, Z.; Liu, J.; Li, T.; Wang, B.; Yang, Z. A simple route to $CoFe_2O_4$ nanoparticles with shape and size control and their tunable peroxidase-like activity. *RSC Adv.* **2015**, *5*, 10632−10640.

(18) Zhou, Z.; Zhao, Z.; Zhang, H.; Wang, Z.; Chen, X.; Wang, R.; Chen, Z.; Gao, J. Interplay between Longitudinal and Transverse Contrasts in Fe_3O_4 Nanoplates with (111) Exposed Surfaces. *ACS Nano* **2014**, *8*, 7976−7985.

(19) Chakrapani, K.; Bendt, G.; Hajiyani, H.; Schwarzrock, I.; Lunkenbein, T.; Salamon, S.; Landers, J.; Wende, H.; Schlögl, R.; Pentcheva, R.; Behrens, M.; Schulz, S. Role of Composition and Size of Cobalt Ferrite Nanocrystals in the Oxygen Evolution Reaction. *ChemCatChem* **2017**, *9*, 2988−2995.

(20) Vadivel, M.; Babu, R. R.; Arivanandhan, M.; Ramamurthi, K.; Hayakawa, Y. Role of SDS surfactant concentrations on the structural, morphological, dielectric and magnetic properties of $CoFe_2O_4$ nanoparticles. *RSC Adv.* **2015**, *5*, 27060−27068.

(21) Pereira, C.; Pereira, A. M.; Fernandes, C.; Rocha, M.; Mendes, R.; Fernández-García, M. P.; Guedes, A.; Tavares, P. B.; Grenèche, J. M.; Araújo, J. P.; Freire, C. Superparamagnetic MFe_2O_4 (M = Fe, Co, Mn) Nanoparticles: Tuning the Particle Size and Magnetic Properties through a Novel One-Step Coprecipitation Route. *Chem. Mater.* **2012**, *24*, 1496−1504.

(22) Effenberger, F. B.; Carbonari, A. W.; Rossi, L. M. The influence of 1,2-alkanediol on the crystallinity of magnetite nanoparticles. *J. Magn. Magn. Mater.* **2016**, *417*, 49−55.

(23) Hu, L.; Peng, Q.; Li, Y. Selective Synthesis of Co_3O_4 Nanocrystal with Different Shape and Crystal Plane Effect on Catalytic Property for Methane Combustion. *J. Am. Chem. Soc.* **2008**, *130*, 16136−16137.

(24) Chen, J. S.; Zhu, T.; Hu, Q. H.; Gao, J.; Su, F.; Qiao, S. Z.; Lou, X. W. Shape-controlled synthesis of cobalt-based nanocubes, nanodiscs, and nanoflowers and their comparative lithium-storage properties. *ACS Appl. Mater. Interfaces* **2010**, *2*, 3628−3635.

(25) Chakrapani, K.; Bendt, G.; Hajiyani, H.; Lunkenbein, T.; Greiner, M. T.; Masliuk, L.; Salamon, S.; Landers, J.; Schlögl, R.; Wende, H.; Pentcheva, R.; Schulz, S.; Behrens, M. The Role of Composition of Uniform and Highly Dispersed Cobalt Vanadium Iron Spinel Nanocrystals for Oxygen Electrocatalysis. *ACS Catal.* **2018**, *8*, 1259−1267.

(26) Anke, S.; Bendt, G.; Sinev, I.; Hajiyani, H.; Antoni, H.; Zegkinoglou, I.; Jeon, H.; Pentcheva, R.; Roldan Cuenya, B.; Schulz, S.; Muhler, M. Selective 2-Propanol Oxidation over Unsupported Co_3O_4 Spinel Nanoparticles: Mechanistic Insights into Aerobic Oxidation of Alcohols. *ACS Catal.* **2019**, *9*, 5974−5985.

(27) El Arrassi, A.; Liu, Z.; Evers, M. V.; Blanc, N.; Bendt, G.; Saddeler, S.; Tetzlaff, D.; Pohl, D.; Damm, C.; Schulz, S.; Tschulik, K. Intrinsic Activity of Oxygen Evolution Catalysts Probed at Single $CoFe_2O_4$ Nanoparticles. *J. Am. Chem. Soc.* **2019**, *141*, 9197−9201.

(28) Anke, S.; Falk, T.; Bendt, G.; Sinev, I.; Hävecker, M.; Antoni, H.; Zegkinoglou, I.; Jeon, H.; Knop-Gericke, A.; Schlögl, R.; Roldan Cuenya, B.; Schulz, S.; Muhler, M. On the reversible deactivation of cobalt ferrite spinel nanoparticles applied in selective 2-propanol oxidation. *J. Catal.* **2020**, *382*, 57−68.

(29) Mourdikoudis, S.; Liz-Marzán, L. M. Oleylamine in Nanoparticle Synthesis. *Chem. Mater.* **2013**, *25*, 1465−1476.

(30) Wagner, C. Theorie der Alterung von Niederschlägen durch Umlösen (Ostwald-Reifung). *Z. Elektrochem., Ber. Bunsenges. Phys. Chem.* **1961**, *65*, 581−591.

(31) Sharifi Dehsari, H.; Halda Ribeiro, A.; Ersöz, B.; Tremel, W.; Jakob, G.; Asadi, K. Effect of precursor concentration on size

evolution of iron oxide nanoparticles. *CrystEngComm* **2017**, *19*, 6694−6702.

(32) Miguel-Sancho, N.; Bomati-Miguel, O.; Roca, A. G.; Martinez, G.; Arruebo, M.; Santamaria, J. Synthesis of Magnetic Nanocrystals by Thermal Decomposition in Glycol Media: Effect of Process Variables and Mechanistic Study. *Ind. Eng. Chem. Res.* **2012**, *51*, 8348−8357.

(33) Hansen, T. W.; Delariva, A. T.; Challa, S. R.; Datye, A. K. Sintering of Catalytic Nanoparticles: Particle Migration or Ostwald Ripening? *Acc. Chem. Res.* **2013**, *46*, 1720−1730.

(34) Henrich, V. E. *The Surface Science of Metal Oxides*; Cambridge University Press, 1994; p 36.

(35) Uskaikar, H. P.; Shetti, N. P.; Malode, S. J. Electrocatalytic reduction of oxygen on Co_3O_4: Effects of processing method. *Mater. Sci. Energy Technol.* **2018**, *1*, 129−135.

(36) Sidhureddy, B.; Dondapati, J. S.; Chen, A. Shape-controlled synthesis of Co_3O_4 for enhanced electrocatalysis of the oxygen evolution reaction. *Chem. Commun.* **2019**, *55*, 3626−3629.

(37) Ismail, H. M. A thermoanalytic study of metal acetylacetonates. *J. Anal. Appl. Pyrolysis* **1991**, *21*, 315−326.

(38) Vasvári, G.; Hajdu, P.; Gál, D. Thermal Decomposition and Autoxidation of Cobalt Acetylacetonates. *J. Chem. Soc., Dalton Trans.* **1974**, *5*, 465−470.

(39) von Hoene, J.; Charles, R. G.; Hickam, W. M. Thermal Decomposition of Metal Acetylacetonates: Mass Spectrometer Studies. *J. Phys. Chem.* **1958**, *62*, 1098−1101.

(40) Vasvári, G.; Hajdu, P.; Gál, D. Thermal Decomposition and Autoxidation of Cobalt Acetylacetonates. *J. Chem. Soc., Dalton Trans.* **1974**, *5*, 465−470.

(41) Lalancette, R. A.; Syzdek, D.; Grebowicz, J.; Arslan, E.; Bernal, I. The thermal decomposition and analyses of metal tris-acetylacetonates. *J. Therm. Anal. Calorim.* **2019**, *135*, 3463−3470.

(42) Wanjun, T.; Donghua, C. Mechanism of thermal decomposition of cobalt acetate tetrahydrate. *Chem. Pap.* **2007**, *61*, 329−332.

(43) Yang, J.; Liu, H.; Martens, W. N.; Frost, R. L. Synthesis and Characterization of Cobalt Hydroxide, Cobalt Oxyhydroxide, and Cobalt Oxide Nanodiscs. *J. Phys. Chem. C* **2010**, *114*, 111−119.

(44) Markov, L.; Petrov, K.; Petkov, V. On the thermal decomposition of some cobalt hydroxide nitrates. *Thermochim. Acta* **1986**, *106*, 283−292.

(45) Brust, M.; Walker, M.; Bethell, D.; Schiffrin, D. J.; Whyman, R. Synthesis of Thiol-derivatised Gold Nanoparticles in a Two-phase Liquid-Liquid System. *J. Chem. Soc., Chem. Commun.* **1994**, *7*, 801−802.

(46) Hofmann, D. M.; Fairbrother, D. H.; Hamers, R. J.; Murphy, C. J. Two-Phase Synthesis of Gold-Copper Bimetallic Nanoparticles of Tunable Composition: Toward Optimized Catalytic CO_2 Reduction. *ACS Appl. Nano Mater.* **2019**, *2*, 3989−3998.

(47) Wang, Y. J.; Hu, P.; Ma, X. L. Oxygen Reduction Reaction on Metal-Terminated $MnCr_2O_4$ Nano-octahedron Catalyzing MnS Dissolution in an Austenitic Stainless Steel. *J. Phys. Chem. C* **2011**, *115*, 4127−4133.

(48) Xia, Y.; Xiong, Y.; Lim, B.; Skrabalak, S. E. Shape-controlled synthesis of metal nanocrystals: simple chemistry meets complex physics? *Angew. Chem., Int. Ed.* **2009**, *48*, 60−103.

(49) Qiu, B.; Guo, W.; Liang, Z.; Xia, W.; Gao, S.; Wang, Q.; Yu, X.; Zhao, R.; Zou, R. Fabrication of Co_3O_4 nanoparticles in thin porous carbon shells from metal-organic frameworks for enhanced electro-chemical performance. *RSC Adv.* **2017**, *7*, 13340−13346.

(50) Lukashuk, L.; Yigit, N.; Li, H.; Bernardi, J.; Föttinger, K.; Rupprechter, G. Operando XAS and NAP-XPS investigation of CO oxidation on meso- and nanoscale CoO catalysts. *Catal. Today* **2019**, *336*, 139−147.

(51) Biesinger, M. C.; Payne, B. P.; Grosvenor, A. P.; Lau, L. W. M.; Gerson, A. R.; Smart, R. S. C. Resolving surface chemical states in XPS analysis of first row transition metals, oxides and hydroxides: Cr, Mn, Fe, Co and Ni. *Appl. Surf. Sci.* **2011**, *257*, 2717−2730.

(52) Zou, R.; Xu, K.; Wang, T.; He, G.; Liu, Q.; Liu, X.; Zhang, Z.; Hu, J. Chain-like $NiCo_2O_4$ nanowires with different exposed reactive planes for high-performance supercapacitors. *J. Mater. Chem. A* **2013**, *1*, 8560−8566.

(53) Jin, H.; Wang, J.; Su, D.; Wei, Z.; Pang, Z.; Wang, Y. In situ Cobalt−Cobalt Oxide/N-Doped Carbon Hybrids As Superior Bifunctional Electrocatalysts for Hydrogen and Oxygen Evolution. *J. Am. Chem. Soc.* **2015**, *137*, 2688−2694.

(54) Wang, H. Y.; Hung, S. F.; Chen, H. Y.; Chan, T. S.; Chen, H. M.; Liu, B. In Operando Identification of Geometrical-Site-Dependent Water Oxidation Activity of Spinel Co_3O_4. *J. Am. Chem. Soc.* **2016**, *138*, 36−39.

(55) He, D.; Song, X.; Li, W.; Tang, C.; Liu, J.; Ke, Z.; Jiang, C.; Xiao, X. Active Electron Density Modulation of Co_3O_4-Based Catalysts Enhances their Oxygen Evolution Performance. *Angew. Chem., Int. Ed.* **2020**, *59*, 6929−6935.

(56) Suen, N. T.; Hung, S. F.; Quan, Q.; Zhang, N.; Xu, Y. J.; Chen, H. M. Electrocatalysis for the oxygen evolution reaction: recent development and future perspectives. *Chem. Soc. Rev.* **2017**, *46*, 337−365.